


Article

Design of Three-Dimensional Electrical Impedance Tomography System for Rock Samples

Xin Peng^{1,2}, Shaoheng Chun^{2,3}, Benyu Su⁴, Rujun Chen^{1,2,5,6,*} , Shenglan Hou^{1,2}, Chao Xu^{1,2}
and Haojie Zhang^{1,2}

¹ School of Geoscience and Info-Physics, Central South University, Changsha 410083, China; xinpeng7106@163.com (X.P.)

² AIoT Innovation and Entrepreneurship Education Center for Geology and Geophysics, Central South University, Changsha 410083, China; chunsh123@126.com

³ Control Technology Institute, Wuxi Institute of Technology, Wuxi 214121, China

⁴ School of Resources and Geosciences, China University of Mining and Technology, Xuzhou 221116, China

⁵ Key Laboratory of Metalorganic Prediction of Nonferrous Metals and Geological Environment Monitoring (Central South University), Ministry of Education, Changsha 410083, China

⁶ Hunan Key Laboratory of Non-Ferrous Resources and Geological Hazard Detection, Changsha 410083, China

* Correspondence: chrujun@csu.edu.cn; Tel.: +86-137-8708-0374

Abstract: Research on the electrical properties of rocks and ores plays a crucial role in the development of geophysical electromagnetism methods. However, currently available instruments suffer from high power consumption, a limited number of electrodes, inaccurate measurements, poor portability, and a limited ability to measure the electrical parameters of rocks and ores. To address these issues, this paper presents a three-dimensional electrical impedance tomography system for rock samples with high-density microelectrodes based on an Android system and STM32 microcontroller. The system features high observation accuracy, dense electrode arrays (with 384 current and potential electrodes), flexible electrode selection, user-friendly human–computer interaction, good stability, and real-time performance. Powered by a single power bank, the entire instrument can be controlled and monitored wirelessly via Bluetooth and Wi-Fi technology using an Android smartphone. Additionally, the system not only enables accurate measurement of electrical parameters, but also facilitates the generation of three-dimensional impedance imaging of specimens via inversion algorithms after data export, allowing for a comprehensive understanding of the electrical properties of rocks and ores. This system holds great potential for future research in this field.

Keywords: rock and ore; electrical impedance tomography; STM32; dense electrode arrays



Citation: Peng, X.; Chun, S.; Su, B.; Chen, R.; Hou, S.; Xu, C.; Zhang, H. Design of Three-Dimensional Electrical Impedance Tomography System for Rock Samples. *Appl. Sci.* **2024**, *14*, 1671. <https://doi.org/10.3390/app14041671>

Academic Editor: Filippos Vallianatos

Received: 27 December 2023

Revised: 8 February 2024

Accepted: 17 February 2024

Published: 19 February 2024



Copyright: © 2024 by the authors. Licensee MDPI, Basel, Switzerland. This article is an open access article distributed under the terms and conditions of the Creative Commons Attribution (CC BY) license (<https://creativecommons.org/licenses/by/4.0/>).

1. Introduction

The electrical properties of rocks and ores constitute fundamental prerequisites for electrical (and electromagnetic) field surveys in geophysical exploration [1]. Through these electrical properties, we can understand the differences in resistivity and polarization between mineralized bodies and surrounding rocks, which serve as essential criteria for selecting appropriate geophysical exploration methods. Furthermore, the electrical parameters of rocks and ores provide an objective basis for forward calculations and inversion interpretations, as well as a physical foundation for result explanations [2]. In addition to laboratory-based investigations, the study of rocks and ores often necessitates field-based research. For example, the practice of metal ore exploration often involves splitting key core samples along the core axis, reserving one portion for laboratory analysis while preserving the other as evidence of exploration. Consequently, there are situations where it becomes imperative to conduct measurements on specific core samples within their original field environment before the splitting procedure takes place [3]. Consequently, the development of a highly precise, portable, and efficient instrument system for obtaining

accurate and reliable electrical information from rock and ore specimens represents a crucial foundational research area in geophysical instrument development [4]. Currently, the focus of researchers lies predominantly on the measurement of the overall electrical properties of rock and ore specimens, while the study of three-dimensional impedance imaging techniques capable of reconstructing the internal impedance distribution within such specimens remains relatively limited.

In 2009, GDD Instrumentation Company in Canada developed the Sample Core IP Tester (SCIP), a rock core testing instrument, with the operating software installed on a PDA. This instrument enables rapid real-time measurement of the resistivity and chargeability of sampled specimens, core samples, outcrop rocks, and borehole surrounding rocks [5]. Wang et al. (2014) studied theoretical methods for testing the true electrical parameters of rock and ore specimens and subsequently developed the WXE type test system electrical parameters of rocks and minerals [6]. In 2016, He et al., from Central South University, designed a spectral induced polarization measurement system for high-impedance rock and ore samples in laboratory settings [7]. Cheng et al. (2021) developed a precise current encoding signal transmitting system for measuring electrical parameters of rock and ore specimens [8]. In 2022, Gurin et al. conducted high-precision laboratory measurements of spectral induced polarization (SIP) on rock samples using the multi-functional electrochemical P-40× potentiostat-galvanostat instrument [9]. However, the aforementioned instruments can only conduct overall measurements of the electrical parameters of rock and ore specimens and lack the capability to obtain a visual three-dimensional distribution of electrical impedance.

Electrical impedance tomography (EIT) refers to a non-invasive imaging technique that involves applying electrical signals to a target object, observing boundary voltage data on the surface of the object, and then using inversion algorithms to reconstruct the internal conductivity distribution of the target object [10]. This efficient and non-destructive imaging technique has been widely applied in medical diagnostics [11,12] (such as lung and breast examinations) and material inspections [13]. Additionally, it is increasingly being used to characterize the structure of underground systems. For example, in 2022, Weigand et al., from the University of Bonn in Germany, designed spectral electrical impedance tomography (sEIT) to characterize the structure of subsurface systems [14]. Therefore, EIT technology provides a new approach for studying rock and ore specimens.

In recent years, with the advancement of electronic technology, Android technology has been widely applied in various geophysical instruments, driving the development of lightweight and intelligent geophysical instruments. Compared to computer-based host systems, Android smartphones offer advantages such as portability, ease of use, aesthetic interfaces, and long battery life, making them more suitable for field exploration in geophysics. For instance, Wen et al. developed acquisition and monitoring software for a Wide-Field electromagnetic receiver based on the Android platform [15].

Building upon the aforementioned research, this study developed an electrical impedance tomography system for rock samples with high-density microelectrodes. The system incorporates low-power and high-precision devices such as the STM32 microcontroller and CPLD (Complex Programmable Logic Device) to ensure measurement accuracy and reduce power consumption. Human-machine interaction is achieved through an Android smartphone, enabling real-time monitoring of the instrument's operational status and facilitating user convenience. Consequently, the need for conventional display panels used in most geophysical instruments is eliminated, resulting in reduced power consumption, improved instrument sealing, and decreased weight. Bluetooth and Wi-Fi wireless communication technologies are employed to eliminate the time-consuming and laborious process of laying cables in challenging terrain conditions, which often leads to tangles, disconnections, and short circuits. The system is designed with 192 current electrodes and 192 potential electrodes, surpassing the typical 16-electrode configuration [16] and 32-electrode configuration [17] used in most EIT systems. This increased electrode count ensures a comprehensive coverage of rock and ore specimens. All electrode channels can

be flexibly selected and configured on the Android App according to specific requirements. Once the electrodes are initially deployed, automatic switching and data acquisition can be achieved, enhancing measurement efficiency and increasing the volume of acquired data. Subsequently, three-dimensional inversion imaging of rock and ore specimens can be performed based on the collected data, allowing for a comprehensive representation of their electrical properties. Furthermore, this system also enables fully automated three-dimensional high-density induced polarization imaging of target bodies in water tanks, facilitating related research in electrical exploration. The system can also carry out detailed three-dimensional detection of tree and crop roots [18,19].

2. Principle and Methods

In the practical measurement process, the initial step entails determining the suitable number of electrodes based on the characteristics of the targeted rock or ore specimen, including parameters such as the base diameter and height. Insufficient electrode quantity impedes the acquisition of ample data, hindering a comprehensive reflection of the electrical properties of the rock or ore. Conversely, an excessive number of electrodes results in extended measurement time without a commensurate improvement in measurement precision. Subsequently, a judicious arrangement of electrodes is required. The schematic diagram depicting the operation of the instrument is illustrated in Figure 1. The positive terminal of the signal source incorporated in our instrument is linked to the current electrodes, serving the purpose of delivering a consistent voltage or current signal to the rock or ore specimen. Following this, the negative terminal of the signal source is interconnected with the central region of the lower surface of the rock or ore specimen, having been serially connected with a high-precision sampling resistor. The ellipsis in the figure denotes the prospective arrangement of additional electrodes based on particular circumstances. During operation, each current electrode activates in sequence, with the corresponding set of potential electrodes (Every five are grouped together) conducting data collection and switching. Once the potential electrode switching is completed, the next current electrode initiates its operation, and the potential electrodes repeat their previous cycle. The measurement concludes upon the completion of the operation of all current electrodes. The electrode arrangement method employed in this study introduces a streamlined and convenient procedure for configuring electrodes, concomitantly diminishing measurement time and enhancing the efficiency of data collection. This approach confers distinct advantages, especially considering the significant quantity of electrodes within our system. Given the dual-purpose design of our system for laboratory and field measurements, this method amplifies its adaptability to intricate topographical conditions. For instance, in the subsequent experiments detailed in this paper, we opted for 48 current electrodes and 48 potential electrodes, distributed across four horizontal planes and 24 vertical lines spaced at 15° intervals.

For rock samples with lower resistance values, a constant current source measurement method is utilized to avoid generating large currents within the circuit, which could increase power consumption and damage circuit components. Conversely, for rock samples with higher resistance values, a constant voltage source measurement method is employed to mitigate the influence of smaller currents on measurement accuracy.

The system directly acquires voltage and current data. Subsequently, we applied fast Fourier transform (FFT) to convert the time-domain signal into the frequency-domain signal, enabling us to compute impedance and phase results from the obtained complex numbers.

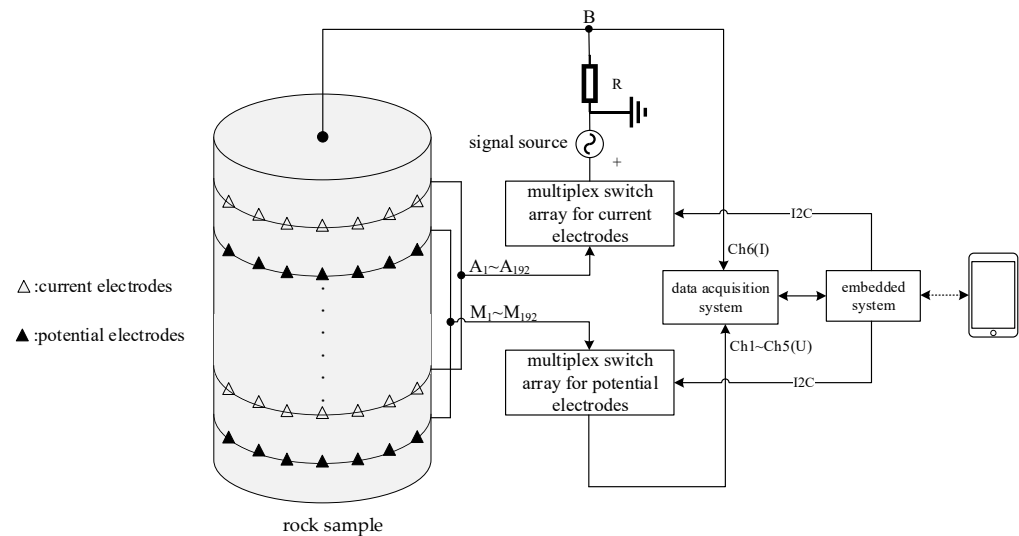


Figure 1. Schematic diagram depicting the operation of the instrument.

After the system measurement is completed, the raw data collected by the Android software are exported for inversion processing [20].

In the process of forward modeling, we utilized the finite element numerical simulation method to simulate cylindrical rock sample. The strength of this approach lies in its adaptability to handle diverse irregular geological models and boundary conditions, along with its ability to tackle intricate non-linear and heterogeneous media.

Based on the Occam smooth inversion [21,22], we performed inversion on the measured data. The inversion objective function is constructed as Equation (1).

$$\Phi = (\Delta \vec{d} - J \vec{m})^T (\Delta \vec{d} - J \vec{m}) + \lambda (R \vec{m})^T (R \vec{m}) \quad (1)$$

where $\Delta \vec{d}$ is the difference between observation data and forward modeling data; \vec{m} is the parameter vector of the model at individual nodes; J is the Jacobian coefficient matrix; and λ is the Lagrange factor, which can be used to control the smoothness of the model. A larger value of λ can prevent abrupt changes in the model's parameters. Initially, a relatively large value is assigned to λ during the inversion process, and as the number of iterations increases, λ gradually decreases; R is the roughness matrix and it is expressed as

$$R = \begin{bmatrix} 0 & \dots & \dots & \dots & \dots & 0 \\ -1 & 1 & 0 & \dots & \dots & \vdots \\ 0 & -1 & 1 & 0 & \dots & \vdots \\ \vdots & & \ddots & \ddots & \ddots & \vdots \\ \vdots & & & \ddots & \ddots & 0 \\ 0 & \dots & \dots & 0 & -1 & 1 \end{bmatrix} \quad (2)$$

The model parameters can be modified using Equation (3):

$$\Delta \vec{m} = (J^T J + \lambda R^T R)^{-1} J \Delta \vec{d} \quad (3)$$

We utilize the root mean square error as a metric to evaluate the similarity between the inversion model and the measured data. The *RMS* is expressed as Equation (4):

$$RMS = \sqrt{\frac{1}{N} \sum_{i=1}^N \left(\frac{d_i - f(\vec{m})_i}{d_i} \right)^2} \times 100 \quad (4)$$

where N is the number of observed data points; d_i represents the i -th observed data value; and RMS denotes the root mean square error. The inversion process stops when the rate of change of *RMS* becomes sufficiently small, satisfying the termination condition.

3. Overall Design Scheme

The system consists of two main components: the control system and the measurement system [23].

The control system comprises an Android application (App) and an embedded system [24]. The Android App serves as the user interface for interacting with the entire instrument. Its primary functions include control, parameter settings, and display of measurement results. The App can also monitor the instrument's operational status by receiving and analyzing log information returned by the instrument during operation. The data stored in the App can be uploaded to the computer for further processing and three-dimensional inversion imaging of the specimens using dedicated software.

The embedded system, powered by an STM32 microprocessor, plays a crucial role in receiving and parsing commands from the App and transmitting them to the measurement system. It also receives the raw data acquired by the measurement system, saves a backup copy to the SD memory card, and uploads it to the App. Additionally, the embedded system controls the relays through the I2C bus.

The measurement system primarily consists of a CPLD acquisition circuit board, a signal source circuit based on the AD9956 core, and two relay circuit boards. It is responsible for data acquisition and meets the design requirements of high precision and low power consumption. Figure 2 depicts the physical layout of the instrument's main hardware circuit boards, including the embedded system, the CPLD, the signal source, the current electrode relays, and the potential electrode relays.

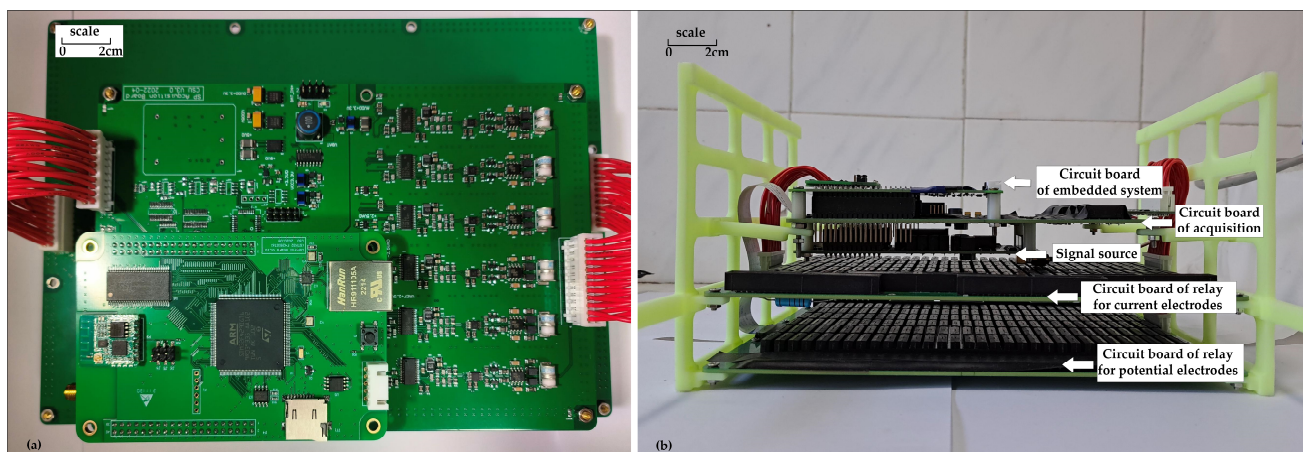


Figure 2. (a) Front view of hardware circuit board. (b) Side view of hardware circuit board.

The physical components of this system consist of an instrument host, high-density cables, a portable rechargeable battery (5 V, 2 A), and an Android smartphone, as shown in Figure 3a. The instrument host panel features electrode interfaces, a power supply interface, and a GPS interface, as depicted in Figure 3.

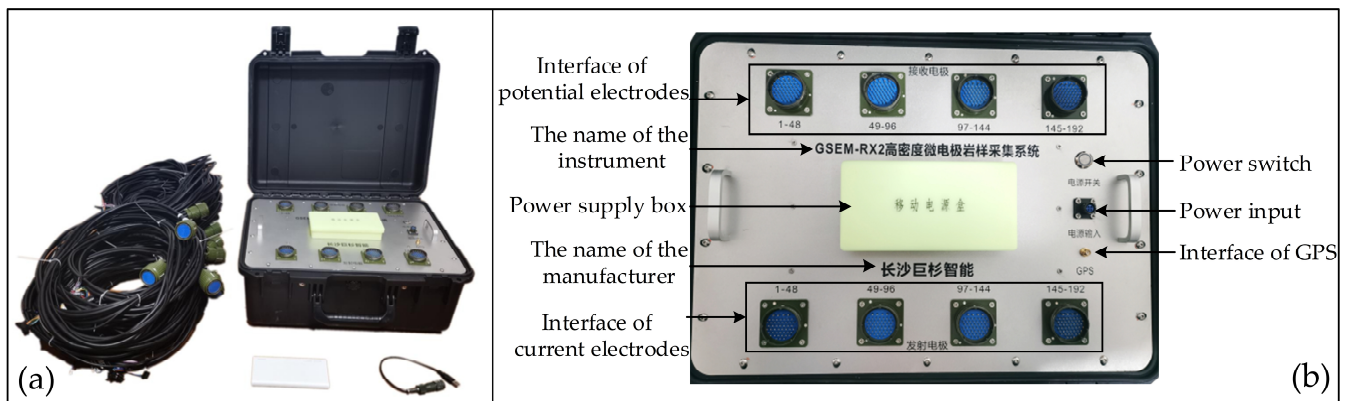


Figure 3. (a) EIT system for rock samples with high-density microelectrode. (b) Interface of host panel.

4. Measurement System

The measurement system primarily consists of the CPLD acquisition circuit board, the signal source circuit board based on AD9956, and two relay circuit boards.

The acquisition circuit board, as shown in Figure 4, is responsible for data acquisition, including modules such as the front-end circuit, ADC circuit, FPGA, and power supply circuit. The acquisition circuit board comprises six channels, consisting of five voltage measurement channels and one current measurement channel. When the signal source supplies an AC signal of a specific frequency to the object under test, the acquisition circuit board can measure the electrical signals at different positions of the object, converting the analog signals into stable digital signals and transmitting them to the embedded system circuit board [25]. It concurrently undertakes the responsibility of receiving commands from the control system through the SPI bus, subsequently parsing them to configure other modules of the measurement system. This configuration facilitates calibration and data acquisition functionalities.

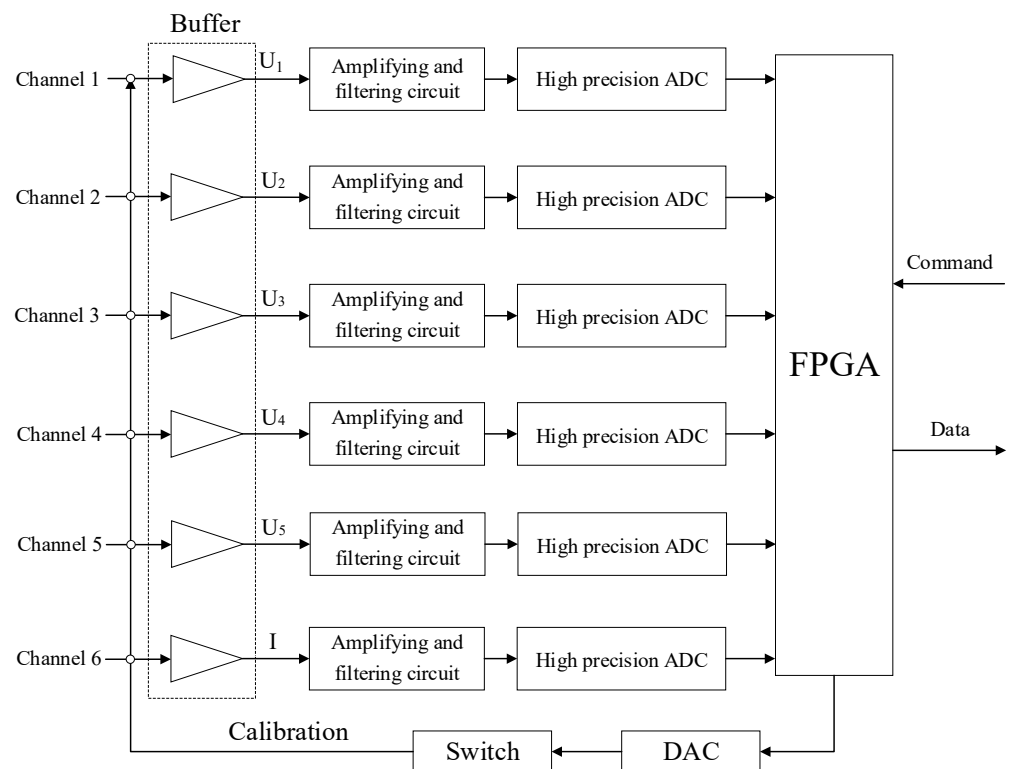


Figure 4. Design structure diagram for the circuit board of acquisition.

To meet the high precision and low power consumption design requirements of the system, the control core of the acquisition board adopts Lattice's MachXO2-2000 ZE CPLD. This series of CPLDs utilizes a 65 nm low-power process with a core supply voltage of 1.2 V and standby power consumption of only 22 μ W. Simultaneously, the onboard resources of the CPLD fully meet the requirements of our design. During the acquisition process, the analog signal is converted into a 32-bit digital signal through the high-precision Analog-to-Digital Converter ADS1282 on the CPLD. The ADS1282 is a low-power, low-noise, and high-precision industrial-grade Analog-to-Digital Converter (ADC) manufactured by Texas Instruments (TI). The ADC incorporates a dual-channel input multiplexer, a low-noise programmable gain amplifier (PGA), and a programmable digital filter. It exhibits outstanding noise immunity and linearity, providing a data sampling rate ranging from 250 SPS to 4000 SPS. The on-chip gain and offset calibration registers support system calibration, making it widely used in geophysical instruments, especially seismic exploration instrument acquisition systems [26].

Figure 5 illustrate the short-circuit input noise data curves of the six channels of the acquisition circuit board at a sampling rate of 1000 SPS and a gain value of 1. It is evident from the illustrated figures that the overall short-circuit noise of the acquisition channels is relatively low, with only minor variations among individual channels, thereby meeting the design specifications.

The signal source circuit board represents a compact, low-power, and broad-amplitude-range signal generator autonomously developed by our research team [27]. This signal generator not only enhances the instrument's portability but also proficiently delivers undistorted excitation to rock or ore specimens with extremely low or high impedance, thereby significantly elevating the precision of the system measurements. Based on the principle of Direct Digital Synthesis (DDS), the signal source converts the digitally generated continuous-time varying signal with a certain pattern (typically a sinusoidal function) into the corresponding analog waveform signal through Digital-to-Analog Conversion. During operation, the configuration of frequency output is accomplished by transmitting frequency control words through the SPI bus, ensuring highly efficient and straightforward frequency control. The signal generator features two operational modes: constant voltage and constant current. In the constant voltage mode, it offers five levels: 10 V, 1 V, 100 mV, 10 mV, and 1 mV, while in the constant current mode, it provides five levels: 10 mA, 1 mA, 100 μ A, 10 μ A, and 1 μ A.

Each of the two relay boards contains 192 relays, with each relay having an interface that connects to an external electrode. The opening and closing of the electrode channels depend on the switching status of the relays. Due to the large number of relays and the limited number of pins on the STM32 chip, the MCP23017 chips are used to expand the IO ports.

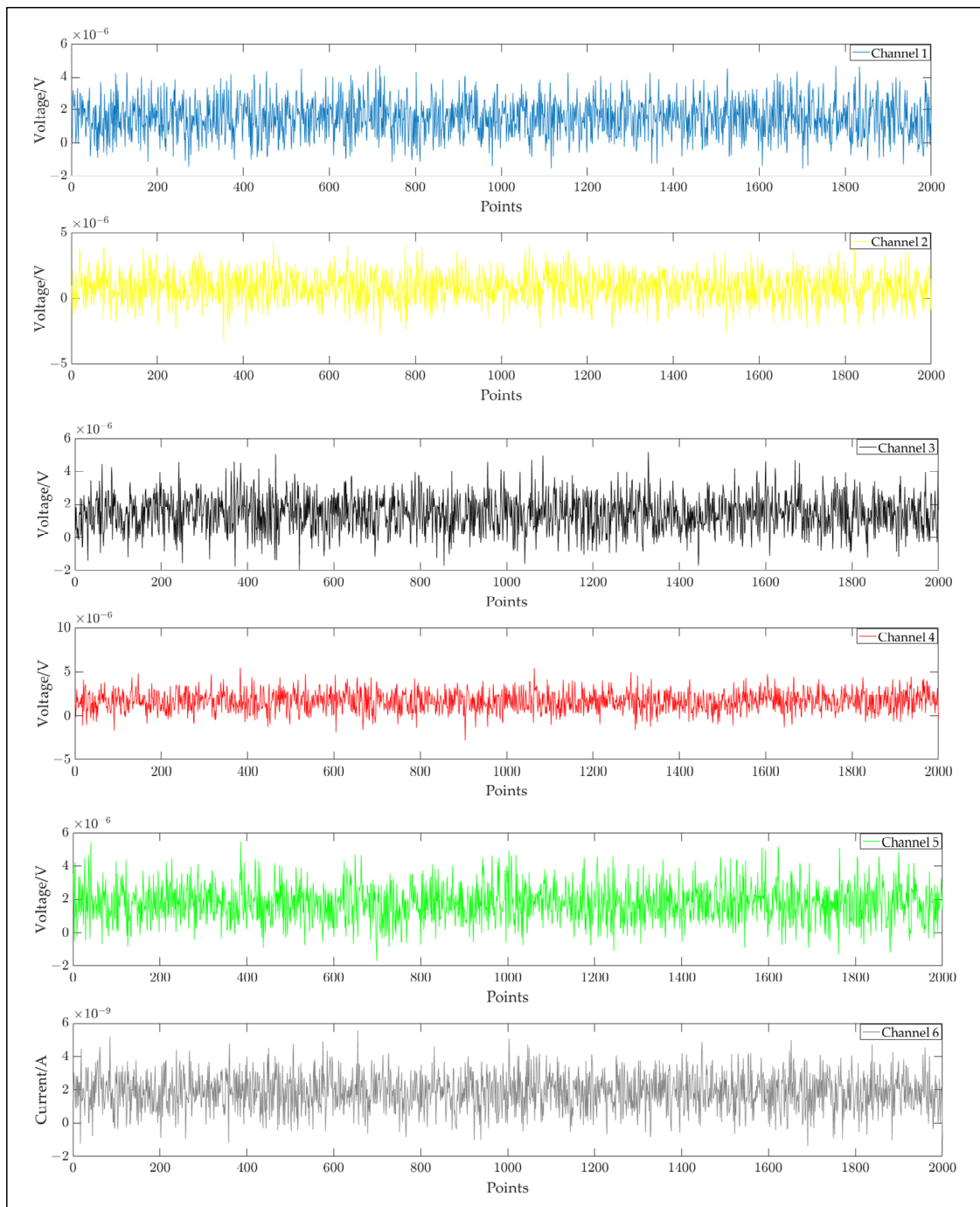


Figure 5. Short-circuit noise curve of six channels.

5. Control System

To meet the requirements of real-time performance and multifunctionality, this design incorporates a lightweight real-time operating system uCOS-III [28] on the STM32 platform. Compared with a bare computer system, RTOS provides an efficient solution for meeting stringent real-time requirements [29,30]. uCOS-III is an operating system specifically designed for controllers with limited onboard hardware resources. It enables function trimming to achieve simplicity by retaining only the necessary features required by the instrument, thereby minimizing resource utilization on the control board.

The software design of the embedded system primarily consists of three parts: a hardware driver for low-level operations, the porting of the operating system, and the application-level task programs running on the operating system.

In the application layer development, the various functions that the embedded system needs to implement are encapsulated into specific tasks. The designed task modules mainly include:

1. **Initialization Task:** This task primarily performs hardware initialization, operating system initialization, and the creation of other tasks. It then starts the task scheduling of the operating system.
2. **Command Parsing Task:** The embedded system receives commands from the Android App through the Bluetooth module. Simultaneously, upon receiving a command, it provides feedback to the Android App to indicate that the command has been received, ensuring stable information transmission. The command information consists of a 64-bit binary stream.
3. **Relay Control Task:** The main functionality of this task is to control the relay switches. As the accurate opening and closing of relays in each measurement directly impact the measurement accuracy of the instrument, a validation mechanism for relays has been designed in the software program.
4. **Data Storage Task:** The embedded system needs to store the measured raw data in an SD memory card to create data backups. Direct Memory Access (DMA) technology is used for data storage. DMA enables high-speed data transfer between peripherals and memory or between memories. Without CPU intervention, data can be moved quickly using DMA, saving CPU resources for other operations.
5. **Data Transmission Task:** Data transmission is conducted through a Wi-Fi module, establishing a stable Transmission Control Protocol (TCP) communication with the Android App.

6. Design of the Android Application

The application serves as the central control core of the entire instrument. To enhance user experience and reduce software learning complexity, the software interface adopts a design style similar to that of WeChat, with navigation tabs for switching between four different screens [31]. The software interface is shown in Figure 6.

The area within the red outline represents the graphical area, which serves the function of displaying the acquisition results as curve graphs on the mobile device. The software incorporates the MPAndroidChart charting library to enable functionalities such as double-click zooming and swipe-to-zoom on the charts. Furthermore, the coordinate axes are automatically adjusted based on the data magnitude. This region encompasses two charts: the first chart presents the raw data acquired, encompassing voltage measurements from five voltage channels and current measurements from one current channel. It employs a dual-axis representation, with the left vertical axis denoting voltage coordinates and the right vertical axis indicating current coordinates. The X-axis corresponds to the number of points computed using the Fourier transform algorithm. The six data sets are displayed in different colors for easy differentiation. The second chart shows the processed results of apparent resistance and phase. In this chart, the left vertical axis represents apparent resistivity, the right vertical axis represents phase, and the X-axis represents the electrode configurations set by the user in the parameter settings interface.

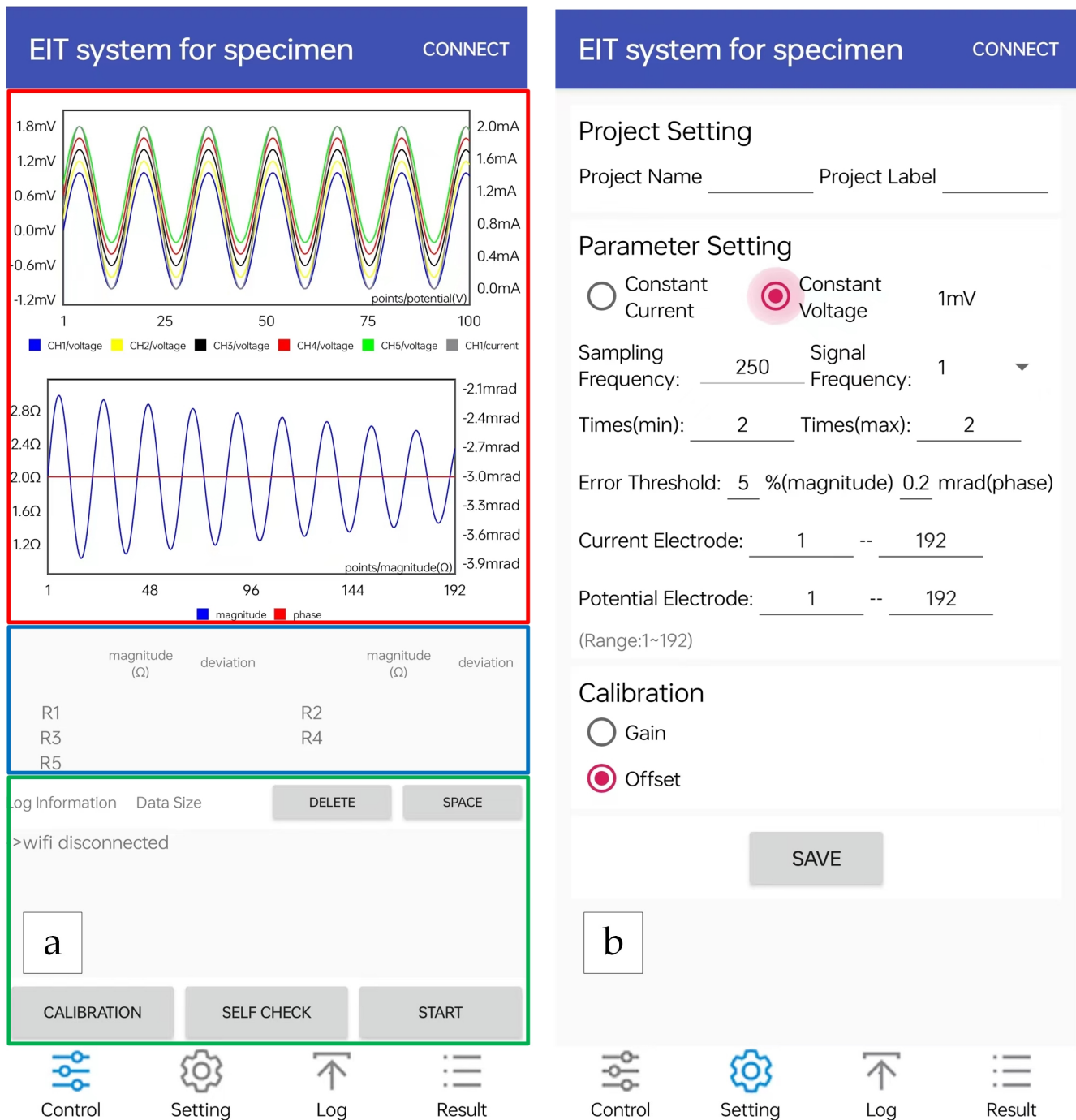


Figure 6. Interface of application. The interface (a) represents the interface of the acquisition and control module, which serves as the main interface of the software and is divided into three sections. (Red, blue, and green outlines are added for annotation and are not part of the actual interface.) The interface (b) illustrates the interface of the parameter settings module, which is divided into three sections: Project Setting, Parameter Setting, and Calibration. In the Parameter Setting module, users can select between two different measurement modes: constant voltage or constant current. They can also specify the magnitude of voltage or current, the sampling frequency, signal frequency, and the time of repeated measurements, as well as the range of potential electrodes and current electrodes. Both the potential electrodes and current electrodes span a range from 1 to 192.

The content within the blue border is presented in the form of a table, providing an accurate display of specific values for apparent resistances and measurement errors.

Within the green border are the functional buttons of the software, including buttons such as “CALIBRATION” and “START”. It also includes buttons for clearing the SD card and viewing the remaining storage space, allowing users to conveniently access the instrument’s storage information at any time.

The log information section displays and stores real-time log information generated during the instrument’s operation. This feature enables users to monitor the instrument’s status and helps identify any issues that may arise.

7. Results

In Table 1, a summary and comparison of performance parameters for typical EIT systems in various application domains are presented.

Table 1. Parameter summary and comparison.

Parameters	FDM-EIT	EIT-40	KIT4	Our System
Publication	[11]	[14]	[32]	
Application Field	Human lung detection	Near-surface monitoring	Industrial analysis	Rock and ore analysis
Current Range	$\pm 20\text{--}200\ \mu\text{A}$	/	/	$\pm 10^4, \pm 10^3, \pm 100, \pm 10, \pm 1\ \mu\text{A}$
Voltage Range	/	$\pm 10\ \text{V}$	$\pm 5, \pm 10\ \text{V}$	$\pm 10^4, \pm 10^3, \pm 100, \pm 10, \pm 1\ \text{mV}$
A/D Converter	16 Bit	24 Bit	14 Bit	32 Bit
Signal	Sinusoidal	Sinusoidal	Arbitrary	Sinusoidal
Power Supply	$\pm 1\ \text{V}$	12 V	/	5 V
Total of Electrodes	16	40	96	384
Man–machine Interaction	PC	PC	PC	Smartphone

/: The symbol “/” represents an unknown parameter.

7.1. Model Test

To validate whether the system meets the design requirements, model testing is conducted as a primary step. In the field of geophysics, the utilization of impedance–capacitance network models, such as the Cole–Cole model [33,34], has been proposed to simulate rock and ore specimens. Hence, in this testing phase, the Cole–Cole model’s relevant theories are employed, and two sets of models (as depicted in Figures 7 and 8) are utilized to evaluate the measurement accuracy of the system.

The testing results of model I are illustrated in Figure 9. The displayed charts in the App depict the graphs illustrating amplitude and phase when the potential electrode labeled as 1 is active. The complete measurement results for the model are presented in Table 2. From the obtained curves, it is evident that the magnitude curve exhibits a smooth increase that aligns closely with theoretical expectations, indicating accurate measurement of the magnitude values at each channel’s corresponding current electrode position. The phase curve oscillates around 0 mrad, aligning closely with the expected phase near zero for a purely resistive model.

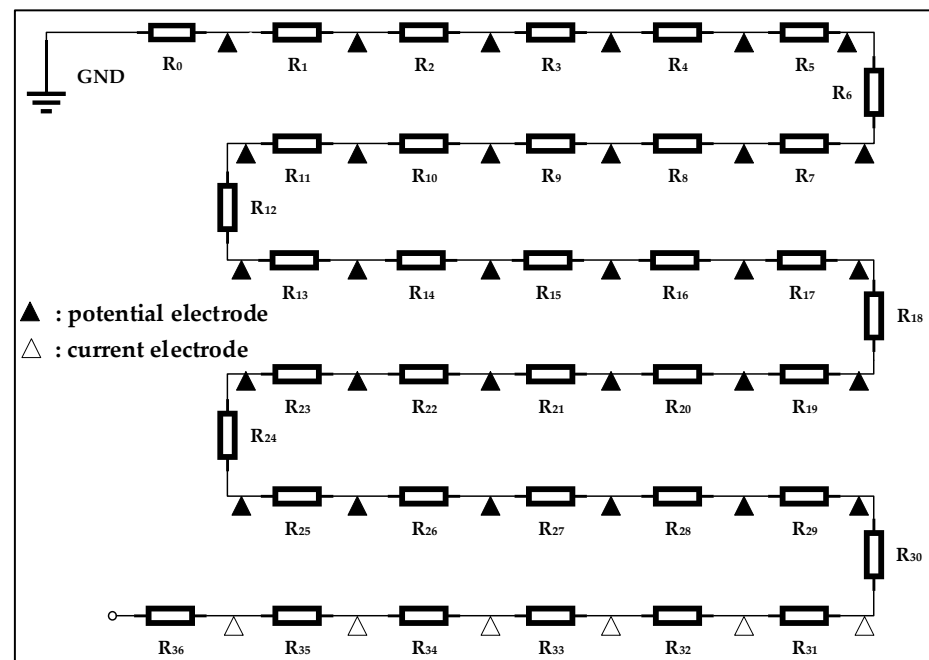


Figure 7. Model I. The resistance values are uniformly set to $1000\ \Omega$. The black triangles represent current electrodes, with current electrode 1–30 selected in this test. Specifically, the current electrode labeled as 1 is located between R_0 and R_1 . On the other hand, the white triangles represent potential electrodes, with potential electrode 1–6 chosen in this test. Specifically, the potential electrode labeled as 1 is positioned between R_{30} and R_{31} .

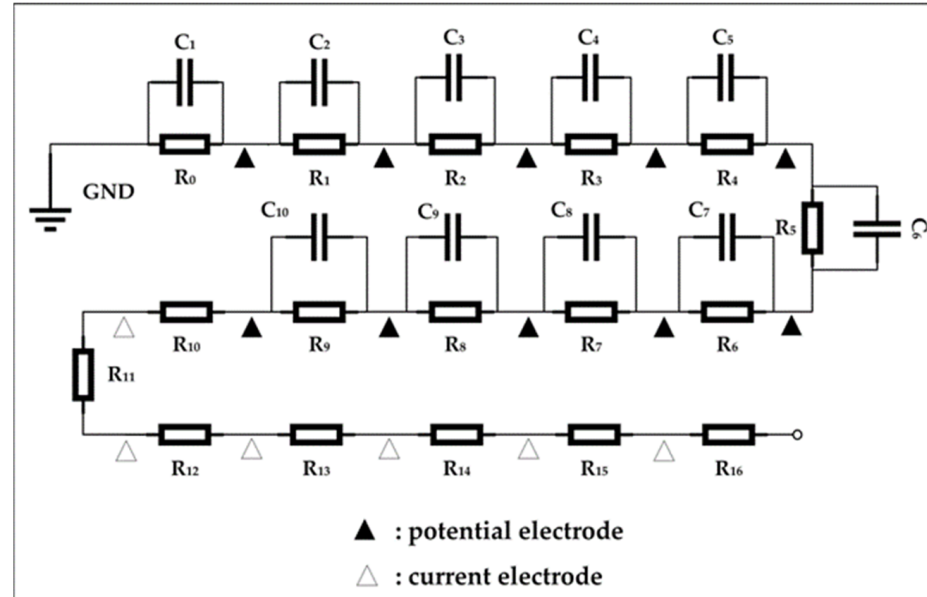


Figure 8. Model II. The resistance values are uniformly set to $1000\ \Omega$ and the capacitance values are uniformly set to $10\ \mu\text{F}$. The black triangles represent current electrodes, with current electrode 1–10 selected in this test. Specifically, the current electrode labeled as 1 is located between R_0 and R_1 . On the other hand, the white triangles represent potential electrodes, with potential electrode 1–6 chosen in this test. Specifically, the potential electrode labeled as 1 is positioned between R_{10} and R_{11} .

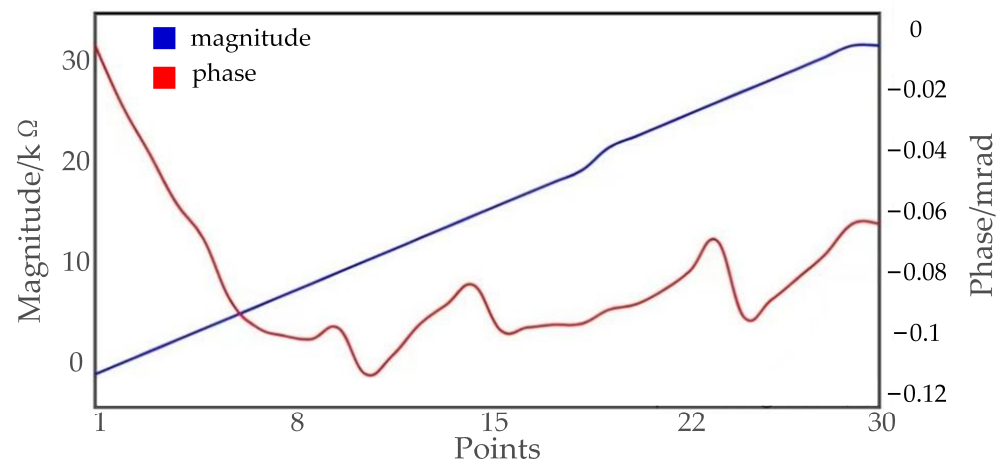


Figure 9. Test result of model I when the potential electrode labeled as 1 is active.

Table 2. Complete measurements of model I when the potential electrode labeled as 1 is active.

Electrode Number	Measured Resistance (Ω)	Theoretical Resistance (Ω)	Deviation (%)	Measured Phase (mrad)	Theoretical Phase (mrad)	Deviation (mrad)
1-1	1003.09	1000	0.31	−0.0092	0	−0.0092
1-2	2002.32	2000	0.12	−0.0281	0	−0.0281
1-3	3003.91	3000	0.13	−0.0432	0	−0.0432
1-4	4001.92	4000	0.05	−0.0590	0	−0.0590
1-5	5000.36	5000	0.01	−0.0702	0	−0.0702
1-6	6002.24	6000	0.04	−0.0897	0	−0.0897
1-7	6998.85	7000	−0.02	−0.0983	0	−0.0983
1-8	7998.05	8000	−0.02	−0.1009	0	−0.1009
1-9	9001.03	9000	0.01	−0.1019	0	−0.1019
1-10	10,003.80	10,000	0.04	−0.0985	0	−0.0985
1-11	11,002.70	11,000	0.02	−0.1130	0	−0.1130
1-12	11,995.84	12,000	−0.03	−0.1071	0	−0.1071
1-13	13,001.93	13,000	0.01	−0.0973	0	−0.0973
1-14	14,008.65	14,000	0.06	−0.0910	0	−0.0910
1-15	15,012.40	15,000	0.08	−0.0849	0	−0.0849
1-16	16,013.65	16,000	0.09	−0.0993	0	−0.0993
1-17	17,001.09	17,000	0.01	−0.0983	0	−0.0983
1-18	17,999.85	18,000	0	−0.0974	0	−0.0974
1-19	19,012.38	19,000	0.07	−0.0971	0	−0.0971
1-20	20,016.28	20,000	0.08	−0.0941	0	−0.0941
1-21	21,015.74	21,000	0.07	−0.0926	0	−0.0926
1-22	21,999.62	22,000	0	−0.0909	0	−0.0909
1-23	23,003.42	23,000	0.01	−0.0865	0	−0.0865
1-24	24,013.22	24,000	0.06	−0.0803	0	−0.0803
1-25	25,017.16	25,000	0.07	−0.0709	0	−0.0709
1-26	26,014.85	26,000	0.06	−0.0951	0	−0.0951
1-27	26,993.44	27,000	−0.02	−0.0896	0	−0.0896
1-28	27,995.92	28,000	−0.01	−0.0825	0	−0.0825
1-29	29,011.80	29,000	0.04	−0.0751	0	−0.0751
1-30	30,019.25	30,000	0.06	−0.0655	0	−0.0655

The testing results of model II are illustrated in Figure 10. The displayed charts in the App depict the graphs illustrating amplitude and phase when the potential electrode labeled as 1 is active. The complete measurement results for the model are presented in Table 3. The results demonstrate high accuracy in data acquisition, with a measurement error of less than 0.3% for resistance and within 1 mrad for phase measurements.

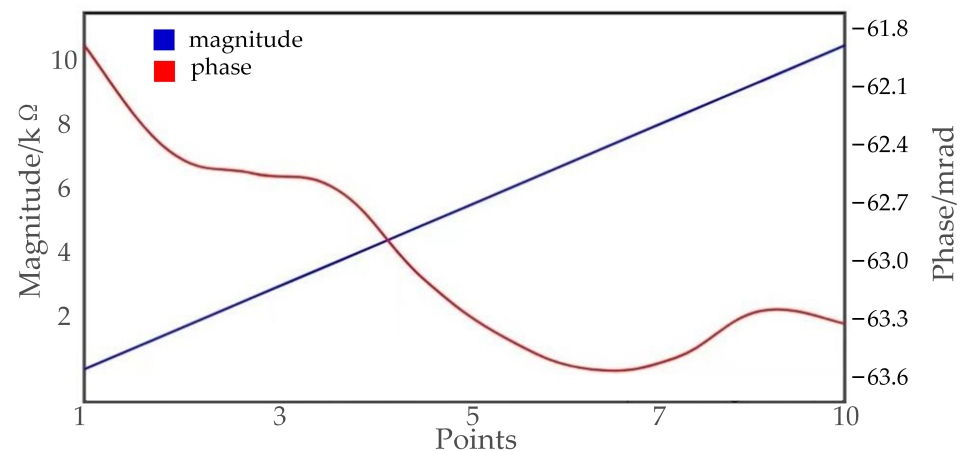


Figure 10. Test result of model II when the potential electrode labeled as 1 is active.

Table 3. Complete measurements of model II when the potential electrode labeled as 1 is active.

Electrode Number	Measured Resistance (Ω)	Theoretical Resistance (Ω)	Deviation (%)	Measured Phase (mrad)	Theoretical Phase (mrad)	Deviation (mrad)
1-1	1000.08	1000	0	−61.95	−62.75	0.8
1-2	1998.87	2000	0.06	−62.50	−62.75	0.25
1-3	2999.94	2999	0.03	−62.57	−62.75	0.18
1-4	3991.17	3999	0.20	−62.65	−62.75	0.10
1-5	4988.49	4999	0.21	−63.08	−62.75	−0.33
1-6	5984.06	5999	0.25	−63.38	−62.75	−0.63
1-7	6984.44	6999	0.21	−63.53	−62.75	−0.78
1-8	7984.52	7999	0.18	−63.47	−62.75	−0.72
1-9	8975.54	8999	0.26	−63.24	−62.75	−0.49
1-10	9978.60	9999	0.20	−63.31	−62.75	−0.56

7.2. Rock and Ore Specimen Test

The previous section's model testing verified the system's high accuracy. To evaluate the system's performance in practical measurements of rock samples, a prototype was used to measure a granite specimen obtained through drilling. The physical specimen is shown in Figure 11, presenting a cylindrical shape with a length of 17 cm and a base diameter of 7 cm. Prior to the measurement, the specimen was soaked in water for 24 h and then removed. The immersion of the rock sample in water before testing served multiple purposes:

- (1) Extended exposure and storage might have led to the formation of an oxide layer on the sample. This layer could potentially diminish the electrical conductivity of the rocks, influencing the accuracy of electrical parameters. Immersing the rock sample effectively eliminated the oxide layer, ensuring more reliable electrical test results.
- (2) The electrical conductivity of certain rocks is closely linked to their water content. Soaking the rock samples increased the water content within the rocks, thereby enhancing their electrical conductivity. This was particularly crucial for measuring specific electrical parameters, as wet rocks closely represented actual underground conditions.
- (3) Rock samples typically exhibit variations in porosity and water absorption properties. Without presoaking the rock samples, different levels of moisture content could lead to variations in measurement results. Uniformly soaking the specimens mitigated this variability, thereby improving the repeatability and accuracy of the measurements.



Figure 11. Granite specimen. (a) The red markings indicate the precise positions of the electrodes. (b) The figure illustrates the specific locations of the cracks within the specimen.

Following the soaking process, the rocks underwent a brief air-drying period. This step aimed to ensure the specimens' surfaces were dry, preventing residual water interference with the measurement results. Due to the cylindrical shape of the specimen, electrode connections were arranged in a circular pattern. At positions 3 cm, 7 cm, 11 cm, and 15 cm (marked in red in Figure 11a), a circular array of electrode connections was established [35], with 24 electrodes in each circle. Among them, the electrodes at positions 3 cm and 11 cm served as potential electrodes, while the other two positions were designated as current electrodes. The grounding electrode was placed at the center of the base [36]. The schematic diagram illustrating the arrangement of electrodes is presented in Figure 12. To enhance electrode–sample coupling, a damp dough was applied at the contact points between each electrode and the specimen. Figure 11b reveals the presence of a noticeable crack in the physical specimen [37].

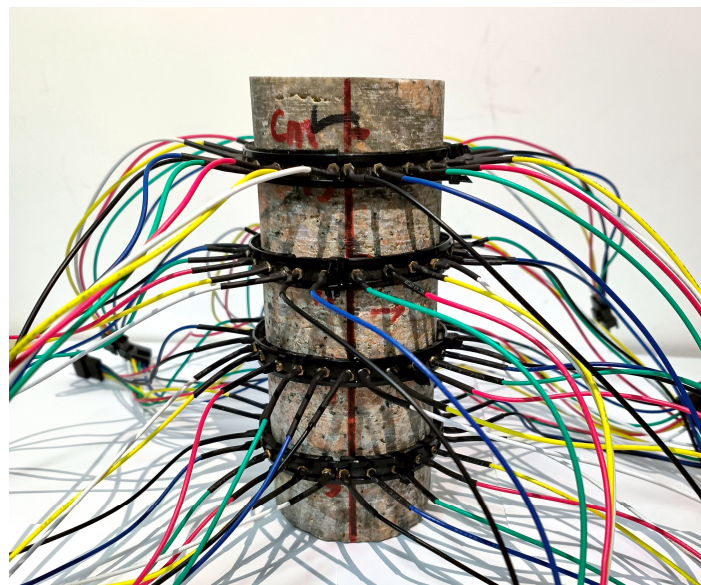


Figure 12. Schematic diagram of the electrode arrangement.

The system is capable of simultaneous acquisition of multiple electrical parameters, enabling the inversion processing of various parameters to fully reflect the electrical characteristics of the rock samples.

Firstly, the three-dimensional resistivity inversion imaging was conducted based on the magnitude and current data. The results are shown in Figure 13. From the inversion results, it can be observed that there is a significant low resistivity zone along the Z-axis at 30–60 mm, which corresponds to the location of the crack on the surface of the specimen. This can be attributed to the decrease in resistivity caused by water-filled cracks. In other positions of the specimen, the resistivity values remain relatively constant and exhibit a uniform distribution, corresponding well with the specimen.

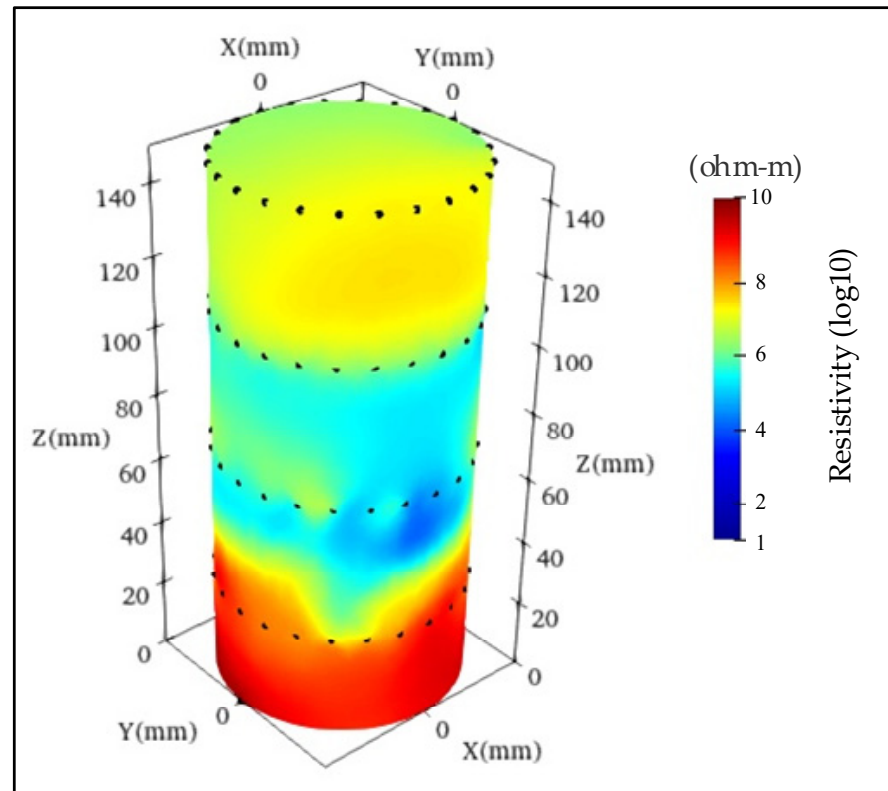


Figure 13. Inversion results of resistivity.

After performing Fourier transform on the raw data, phase data were obtained. Figure 14 shows the inversion results of the phase. In Figure 14a, a three-dimensional segmentation algorithm was applied to the specimen, revealing the phase distribution of the specimen's cross-section. In Figure 14b, a threshold technique was employed to extract high phase values in the fracture zone, providing a better reflection of the fracture locations.

Figure 15 illustrates the inversion results of the resistivity magnitude. Based on the impedance data, the chargeability [38] results can be calculated, as shown in Figure 16. It can be observed that both inversion results reflect the locations of cracks in the specimen. We also observe the presence of a red anomaly in Figure 16. Considering that the sample was not subjected to splitting procedures, we speculate that the presence of the red dots may be indicative of internal variations in density, porosity, moisture content, and other factors relative to the surrounding area.

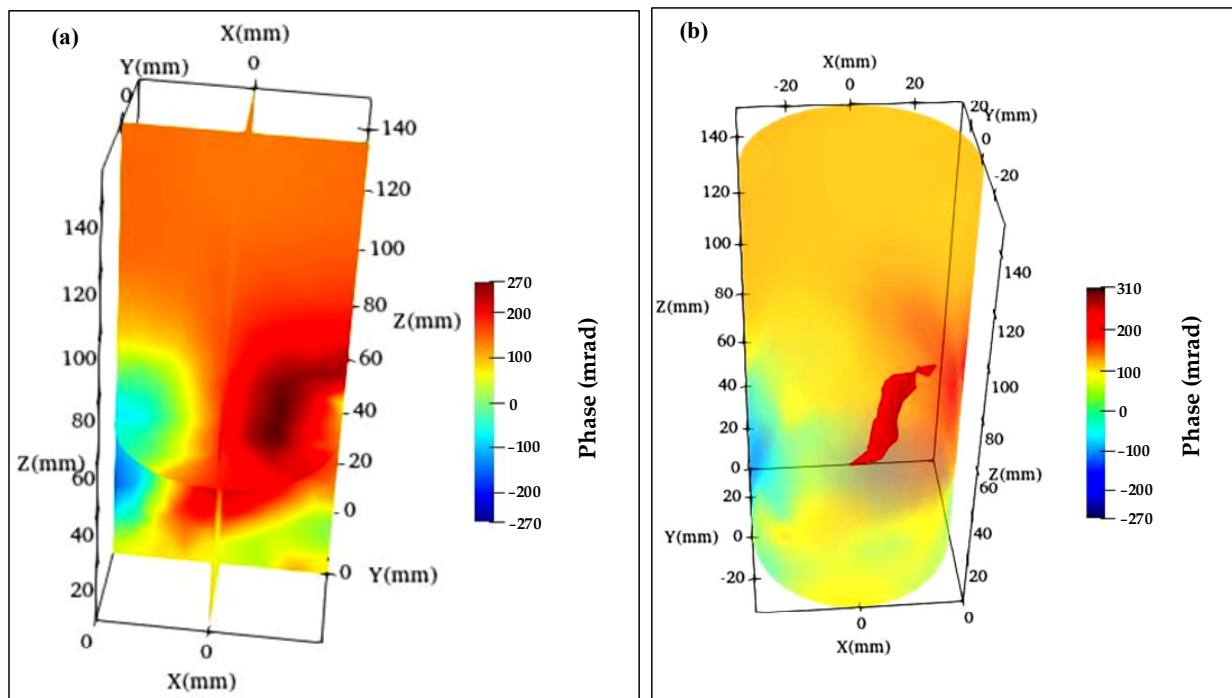


Figure 14. Inversion results of phase. (a) Phase distribution of the specimen's cross-section. (b) Highlighted positions of crack.

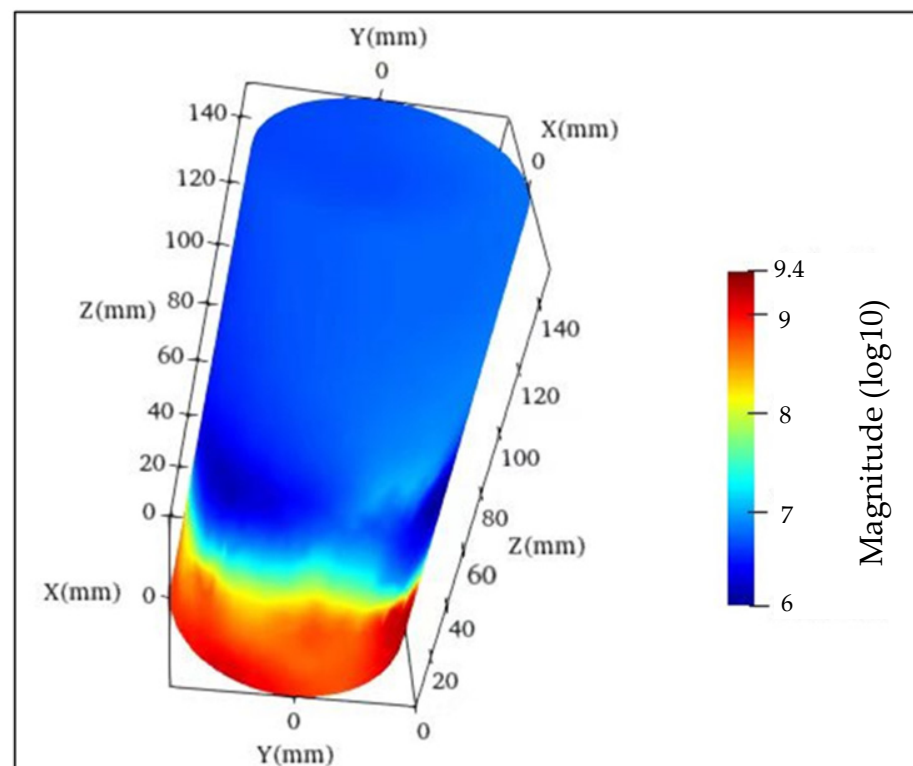


Figure 15. Inversion results of magnitude.

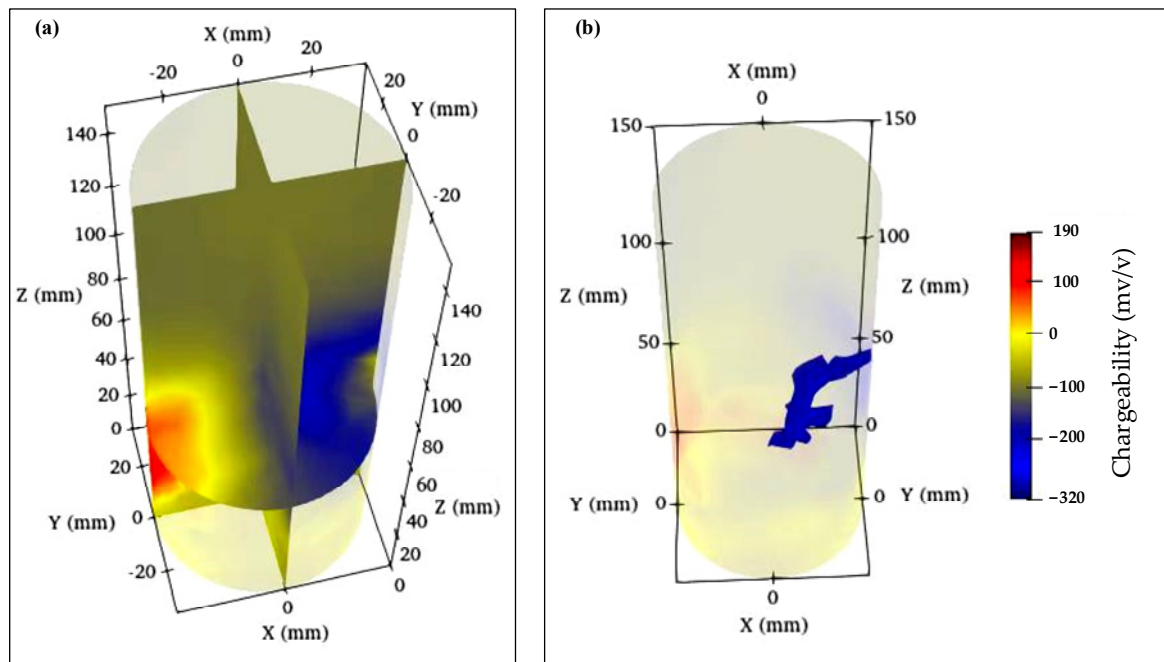


Figure 16. Inversion results of chargeability. (a) Chargeability distribution of the specimen's cross-section. (b) Highlighted positions of crack.

8. Discussion

In our upcoming research, we will endeavor to explore the potential for further minimizing measurement errors and enhancing inversion outcomes by investigating diverse factors including electrode material, electrode dimensions, embedding depth, arrangement, coupling degree, and inversion methodologies.

The measurement of irregularly shaped rock and ore specimens presents a challenge in the field of rock physics, primarily due to decreased coupling between electrodes and rock samples, as well as the inherent difficulty in accurately recording electrode positions. This challenge is particularly pronounced in laboratory-scale experiments, where errors stemming from these factors can significantly impact measurement outcomes. Addressing this issue necessitates specific requirements for both instrument hardware and algorithm design, representing a critical obstacle that our system must overcome.

Our designed system exhibits excellent scalability. Building upon this system, we intend to conduct further research into near-surface geophysics and hydrogeophysics, among other areas.

9. Conclusions

After a comprehensive examination of the current state of research on the electrical properties of rock and ore specimens, this study integrates the latest trends in electronic technology and geophysical instrumentation to design and develop an electrical impedance tomography system for rock samples with high-density microelectrodes based on an Android system and STM32 microcontroller.

The system features a high-density array comprising 384 electrodes, consisting of 192 potential electrodes and 192 current electrodes, allowing for flexible configuration during measurements as needed. We have endeavored to minimize the power consumption of the instrument, thus requiring only a compact power bank for operation. Internally, the instrument incorporates a small-scale signal source designed by us, without compromising accuracy. The integration of smartphones as the interface for human–machine interaction markedly diminishes the complexity entailed in instrument operation.

The testing results demonstrate that the developed acquisition system has successfully met the anticipated design requirements, providing robust technical support for

the investigation of electrical properties in rocks and ore samples. Consequently, this study holds considerable significance in aiding mineral exploration and development by providing valuable assistance in mineralized zone detection, subsurface structure analysis, and mineralization type prediction.

Author Contributions: Conceptualization, R.C., S.C. and B.S.; methodology, R.C. and S.C.; software, X.P., S.H., H.Z. and B.S.; investigation, X.P. and S.C.; resources, X.P. and C.X.; data acquisition and processing, X.P. and B.S.; writing—original draft preparation, X.P.; writing—review and editing, R.C., S.C. and B.S.; visualization, X.P. and B.S.; supervision, R.C.; project administration, S.C.; funding acquisition, R.C. All authors have read and agreed to the published version of the manuscript.

Funding: This research was jointly funded by the National Key R&D Program (2022YFF0706201), the Jiangsu Province Higher Education Basic Science (Natural Science) Research General Project (22KJB510044), the Jiangsu Province “Shuangchuang doctor” Program (JSSCBS20221066) and the school-level doctoral research project (10492722007).

Institutional Review Board Statement: Not applicable.

Informed Consent Statement: Not applicable.

Data Availability Statement: Data is contained within the article, further inquiries can be directed to the corresponding author.

Acknowledgments: We would like to express our gratitude to the research team led by Shiqi Chen, from China University of Mining and Technology, for their assistance in designing and implementing the mainframe mechanical structure of this system. Muyun Tao from China Nonferrous Metals Changsha Investigation and Design Research Institute Co., Ltd. provided support for the experiments in this study. We also extend our thanks to Hongchun Yao and Ruijie Shen, from Central South University, for their valuable support with this research. Additionally, we acknowledge the support and permission granted by Giant Sequoia Artificial Intelligence Technology (Changsha) Limited in making our research findings publicly available.

Conflicts of Interest: The authors declare no conflicts of interest.

References

1. Jia, C.X.; Cheng, H.; Fu, S.Y.; Liao, X.Y.; Zhan, S.Q.; Fu, G.H. High frequency electromagnetic experiment based on spread spectrum coded signals. *Prog. Geophys.* **2023**, 1–10. Available online: <http://kns.cnki.net/kcms/detail/11.2982.P.20231103.1751.049.html> (accessed on 26 December 2023). (In Chinese with English Abstract).
2. Kuwatani, T.; Nagata, K.; Sakai, T.; Iwamori, H. Bayesian Inversion of Lithology and Liquid Phase Parameters from Seismic Velocity and Electrical Conductivity in the Crust and Uppermost Mantle. *J. Geophys. Res. Solid Earth* **2023**, *128*, e2023JB026836. [CrossRef]
3. Mavko, G.; Mukerji, T.; Dvorkin, J. *The Rock Physics Handbook*; Cambridge University Press: Cambridge, UK, 2020.
4. Cheng, H.; Fu, S.Y.; Li, D.Q.; Cui, J.Q.; Liao, X.Y.; Fu, G.H. Research on acquisition method of rock and ore electrical parameters based on IRmPRBS. *Prog. Geophys.* **2022**, *37*, 0374–0385, (In Chinese with English Abstract).
5. Li, L.; Chen, X.D.; Guo, Y.Z. The development of RP-1 instrument for electrical measuring of rocks and minerals. *Geophys. Geochem. Explor.* **2013**, *37*, 529–532, (In Chinese with English Abstract).
6. Wang, Q.Y.; Qiu, G.; Dai, L.; Wang, S.; Xu, L.Z. The development of new test system WXE. *Geophys. Geochem. Explor.* **2014**, *38*, 787–792. (In Chinese with English Abstract).
7. He, X.; Chen, R.J.; Yao, H.C.; Shen, R.J. A complex impedance measurement system for high impedance sample. In Proceedings of the SAGEEP 2016, Denver, CO, USA, 20–24 March 2016.
8. Cheng, H.; Cui, J.Q.; Fu, G.H.; Fu, S.Y.; Zhong, X.Q. Precise current encoding signal transmitting system for measuring electrical parameters of rock and ore. *J. Cent. South Univ. (Sci. Technol.)* **2021**, *52*, 994–1003, (In Chinese with English Abstract).
9. Grigory, G.; Ekaterina, F.; Viacheslav, E.; Evgeniy, K. New equipment for high-accuracy laboratory measurements of spectral induced polarization of rock samples in the time- and frequency domains: Testing of laboratory multifunction potentiostat-galvanostat. *J. Appl. Geophys.* **2022**, *203*, 104703.
10. Leitzke, J.P.; Zangl, H. A Review on Electrical Impedance Tomography Spectroscopy. *Sensors* **2020**, *20*, 5160. [CrossRef]
11. Liu, B.X.; Wang, G.X.; Li, Y.F.; Zeng, L.; Li, H.; Gao, Y.; Ma, Y.X.; Lian, Y.; Heng, C.H. A 13-Channel 1.53-mW 11.28-mm² Electrical Impedance Tomography SoC Based on Frequency Division Multiplexing for Lung Physiological Imaging. *IEEE Trans. Biomed. Circuits Syst.* **2019**, *13*, 938–949. [CrossRef]
12. Mehrnoosh, A.-Z.; Latiff Latiffah, A. Electrical Impedance Tomography as a Primary Screening Technique for Breast Cancer Detection. *Asian Pac. J. Cancer Prev.* **2015**, *16*, 5595–5597.

13. Cagán, J. Hardware implementation of electrical resistance tomography for damage detection of carbon fibre-reinforced polymer composites. *Struct. Health Monit.* **2017**, *16*, 129–141. [CrossRef]
14. Maximilian, W.; Egon, Z.; Valentin, M.; Alexander, H.J.; Andreas, K. Design and operation of a long-term monitoring system for spectral electrical impedance tomography (sEIT). *Geosci. Instrum. Methods Data Syst.* **2022**, *11*, 413–433.
15. Wen, S.S.; Tang, J.T.; Pei, J.; Jiang, Q.Y.; Zhang, B.M.; Li, G. Research and implementation of wide field electromagnetic receiver acquisition monitoring software based on android platform. *Prog. Geophys.* **2018**, *33*, 866–873, (In Chinese with English Abstract).
16. Guo, L. Research and Design of Electrical Impedance Tomography System. Master's Thesis, Jilin University, Changchun, China, 2019. (In Chinese with English Abstract).
17. Mellenthin, M.M.; Mueller, J.L.; de Camargo, E.D.L.B.; de Moura, F.S.; Santos, T.B.R.; Lima, R.G.; Hamilton, S.J.; Muller, P.A.; Alsaker, M. The ACE1 Electrical Impedance Tomography System for Thoracic Imaging. *IEEE Trans. Instrum. Meas.* **2019**, *68*, 3137–3150. [CrossRef] [PubMed]
18. Ehosioke, S.; Garré, S.; Huisman, J.A.; Zimmermann, E.; Placencia-Gomez, E.; Javaux, M.; Nguyen, F. Spectroscopic approach towards unraveling the electrical signature of roots. *J. Geophys. Res. Biogeosci.* **2023**, *128*, e2022JG007281. [CrossRef]
19. Martin, T.; Günther, T. Complex resistivity tomography (CRT) for fungus detection on standing oak trees. *Eur. J. For. Res.* **2013**, *132*, 765–776. [CrossRef]
20. Su, B.Y.; Liu, S.D.; Deng, L.; Gardoni, P.; Grzegorz, M.K.; Li, Z.X. Monitoring Direct Current Resistivity During Coal Mining Process for Underground Water Detection: An Experimental Case Study. *IEEE Trans. Geosci. Remote Sens.* **2022**, *60*, 5915308. [CrossRef]
21. Liu, X.; Ma, H.; Gan, J.J.; Yuan, Z.H. Occam's inversion of 3D tensor CSAMT in data space. *Arab. J. Geosci.* **2023**, *16*, 100.
22. Constable, C.S.; Parker, L.R.; Constable, G.C. Occam's inversion: A practical algorithm for generating smooth models from electromagnetic sounding data. *Geophysics* **2012**, *52*, 289–300. [CrossRef]
23. Zimmermann, E.; Kemna, A.; Berwix, J.; Glaas, W.; Münch, H.M. A high-accuracy impedance spectrometer for measuring sediments with low polarizability. *Meas. Sci. Technol.* **2008**, *19*, 105603. [CrossRef]
24. Zabołotny, M.W.; Kasprowicz, G.; Poźniak, K.; Chernyshova, M.; Czarski, T.; Gaska, M.; Kolasiński, P. FPGA and Embedded Systems Based Fast Data Acquisition and Processing for GEM Detectors. *J. Fusion Energy.* **2019**, *38*, 480–489. [CrossRef]
25. Shen, R.J. Application of FPGA in 3D-SIP System. Master's Thesis, Central South University, Changsha, China, 2012. (In Chinese with English Abstract).
26. Yan, C.; Chen, R.J.; Shen, R.J.; Wu, X.L.; Wang, X.J. Distributed multi-channel data acquisition system for electrical and electromagnetic methods. *Prog. Geophys.* **2021**, *36*, 1743–1750, (In Chinese with English Abstract).
27. Chun, S.H.; Chen, R.J.; Chen, X.S.; Wang, Z.H.; Li, S.J.; Peng, X. Development of signal generator for portable electrical impedance analyzer for rock and ore specimens. *Prog. Geophys.* **2024**, 1–15. Available online: <http://kns.cnki.net/kcms/detail/11.2982.P.20230802.1118.004.html> (accessed on 26 December 2023). (In Chinese with English Abstract).
28. Anonymous. *Micrium and Micrium Adds uC/OS-II and uC/OS-III Support to Energy Micro EFM32 Gecko Microcontrollers*; Defense & Aerospace Business: Auburn, WA, USA, 2010.
29. De Sio, C.; Azimi, S.; Sterpone, L. Evaluating reliability against SEE of embedded systems: A comparison of RTOS and bare-metal approaches. *Microelectron. Reliab.* **2023**, *150*, 115124. [CrossRef]
30. Aviles, P.M.; Lindoso, A.; Belloch, J.A.; Garcia-Valderas, M.; Morilla, Y.; Entrena, L. Radiation testing of a multiprocessor macrosynchronized lockstep architecture with freertos. *IEEE Trans. Nucl. Sci.* **2021**, *69*, 462–469. [CrossRef]
31. Hou, S.L.; Chen, R.J.; Wang, Z.H.; Liu, Z.T.; Liu, J. Development of the NB-IoT-based measurement and control software for broadband SIP response testers for rock and ore specimens. *Geophys. Geochem. Explor.* **2022**, *46*, 1463–1469, (In Chinese with English Abstract).
32. Kourunen, J.; Savolainen, T.; Lehtikainen, A.; Vauhkonen, M.; Heikkinen, L.M. Suitability of a PXI platform for an electrical impedance tomography system. *Meas. Sci. Technol.* **2008**, *20*, 015503. [CrossRef]
33. Hao, W.Y. A Weighting Inversion Method of Spectrum Induced Polarization. *Earth Sci.* **2019**, *8*, 178–189.
34. Liu, W.Q.; Chen, R.J.; Yang, L.Y. Cole-Cole Model Parameter Estimation from Multi-frequency Complex Resistivity Spectrum Based on the Artificial Neural Network. *J. Environ. Eng. Geophys.* **2021**, *26*, 71–77. [CrossRef]
35. Clement, R.; Moreau, S. How should an electrical resistivity tomography laboratory test cell be designed? Numerical investigation of error on electrical resistivity measurement. *J. Appl. Geophys.* **2016**, *127*, 45–55. [CrossRef]
36. Zhong, S.; Wang, Y.; Zheng, Y.; Wu, S.; Chang, X.; Zhu, W. Electrical resistivity tomography with smooth sparse regularization. *Geophys. Prospect.* **2021**, *69*, 1773–1789. [CrossRef]
37. Zhu, W.; Chang, X.; Wang, Y.; Zhai, H.; Yao, Z. Reconstruction of hydraulic fractures using passive ultrasonic travel-time tomography. *Energies* **2018**, *11*, 1321. [CrossRef]
38. Revil, A.; Vaudelet, P.; Su, Z.; Chen, R.J. Induced polarization as a tool to assess mineral deposits: A review. *Minerals* **2022**, *12*, 571. [CrossRef]

Disclaimer/Publisher's Note: The statements, opinions and data contained in all publications are solely those of the individual author(s) and contributor(s) and not of MDPI and/or the editor(s). MDPI and/or the editor(s) disclaim responsibility for any injury to people or property resulting from any ideas, methods, instructions or products referred to in the content.